Photocatalytic Liquid-Phase Selective Hydrogenation of 3-Nitrostyrene to 3-vinylaniline of Various Treated-TiO$_2$ Without Use of Reducing Gas

Okorn Mekasuwandumrong [1], **Saknarin Chaitaworn** [2], **Joongjai Panpranot** [2] and **Piyasan Praserthdam** [2,*]

[1] Department of Chemical Engineering, Faculty of Engineering and Industrial Technology, Silpakorn University, Nakhon Pathom 73000, Thailand; okornm@yahoo.com

[2] Center of Excellence on Catalysis and Catalytic Reaction Engineering, Department of Chemical Engineering, Faculty of Engineering, Chulalongkorn University, Bangkok 10330, Thailand; saknarin362@gmail.com (S.C.); joongjai.p@chula.ac.th (J.P.)

[*] Correspondence: piyasan.p@chula.ac.th; Tel.: +66-2218-6861

check for updates

Abstract: In this work, we investigate the effect of TiO$_2$ properties on the photocatalytic selective hydrogenation of 3-nitrostyrene (3-NS) to 3-vinylaniline (3-VA). The P25-TiO$_2$ photocatalysts were calcined at 600–900 °C using different gases (Air, N$_2$, and H$_2$) and characterized by XRD, N$_2$ physisorption, XPS, UV-Vis, and PL spectroscopy. In the photocatalytic hydrogenation of 3-nitrostyrene in isopropanol, the selectivity of 3-vinylaniline of the treated TiO$_2$ was almost 100%. A linear correlation between the 3-NS consumption rate and PL intensity was observed. Among the catalysts studied, P25-700-air, which possessed the lowest PL intensity, exhibited the highest photocatalytic activity due to the synergistic effect that resulted from its high crystallinity and the optimum amount of anatase/rutile phase content, leading to the reduction of the electron-hole recombination process.

Keywords: photocatalytic 3-nitrostyrene hydrogenation; heat treatment of TiO$_2$; recombination

1. Introduction

The selective hydrogenation of organic molecules is one of the most important goals of the chemical industry. Functionalized anilines produced by hydrogenation of nitroaromatics are the important intermediates in agrochemicals, pharmaceuticals, dyes and pigments. 3-vinylaniline (3-VA) is a significant compound of aniline having a vinyl group and can be used for the production of fine chemicals, functionalized polymers, pigment and pharmaceuticals. Generally, 3-VA is produced by the selective hydrogenation reaction of 3-nitrostyrene (3-NS) [1,2]. This reaction is normally operated under medium-to-high temperature (T > 393 K) and hydrogen pressure (PH$_2$ > 3 bar) using noble metal catalysts [3–5]. The selective hydrogenation of 3-NS to 3-VA is very challenging because there are two reducible functional groups, which could be hydrogenated in 3-NS. The reaction mechanism of 3-NS hydrogenation was proposed by Haber et al. [1]. This process had two different reaction routes, including direct paths to 3-VA and a condensation route. 3-ethylnitrobenzene (3-ENB) and 3-ethylaniline (3-EA) were produced from over-hydrogenation of 3-NS. In order to improve the catalytic performance, the effects of pretreatment conditions [6,7], reaction mediums [6,8], catalyst supports [8,9], and addition of promoters [10] have been investigated.

The photocatalytic reaction process is currently attracting considerable attention due to a myriad of applications, such as hydrogen production by water splitting, air purification, waste water treatment, and selective synthesis of organic compounds [11]. When UV-light is adsorbed by photocatalysts,

the electron in the valence band jumps through the band gap to the conduction band, leaving a positive hole in the former, causing reduction and oxidation, respectively. Among the various photocatalysts, TiO_2 is a common, inexpensive, and non-toxic material that is widely used in many applications as photocatalysts for environmental protection (such as removal of air pollutants, removal of hazardous, disinfection, deodorization and removal of NO_x), and the energy field, for example dye sensitized solar cell and hydrogen evaluation [12–15]. The synthesis of organic compounds by the photocatalytic hydrogenation process at room temperature is an interesting alternative process due to its high safety, indispensable light source, and clean process [2,6].

The production of aniline by photocatalytic hydrogenation of nitroaromatic was reported by Inamura et al. [16–18]. This process can be operated in oxalic acid, formic acid, or alcohol as a hole scavenger with the suspension of TiO_2 at atmospheric pressure and room temperature without the use of any reducing agent. Most research works showed very high aniline selectivity. Moreover, by using alcohol as the solvent and hole scavenger, aniline was produced, in addition to ketone. The effect of reaction conditions, such as the effects of the presence of O_2 and the types of TiO_2 were investigated. However, the effect of TiO_2 properties on the photocatalytic performances in these reactions was not deeply studied. Therefore, this work aims to investigate the effect of TiO_2 properties obtained after treatment under various conditions on the catalytic performances in the liquid phase photocatalytic hydrogenation of 3-NS to 3-VA in 2 propanol under UV light irradiation.
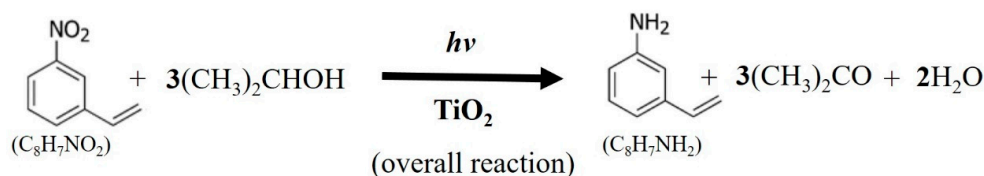
2. Results and Discussion

2.1. Reaction Results

In this work, the effect of TiO_2 properties on the photocatalytic selective hydrogenation of 3-NS to 3-VA was investigated in a batch reactor under UV light irradiation for 6 h without the use of a reduction gas. The photocatalytic performances in terms of %3-NS conversion and %3-VA selectivity on various treated TiO_2 are summarized in Table 1. The 3-NS conversion increased from 45.4% for the non-treated P25 to 70.9% for the TiO_2 calcined at 700 °C in air flow. However, further increase of calcination temperature to 800 °C and 900 °C resulted in the decrease of %3-NS conversion to 57.8 and 51.5, respectively. Changing the calcination gas also affected the photocatalytic activity of TiO_2. The %3-NS conversions increased in order of Air > H_2 > N_2. It is interesting to note that only 3-VA and acetone were observed in this process, which indicated that there were no by-products formed. The %3-VA selectivity of all the treated TiO_2 catalysts were nearly 100%. The formation rate of 3-VA and acetone are shown in Table 1. The formation rate of 3-VA of all the treated catalysts was proportional with the formation rate of acetone at the ratio around 1:3. The reaction equations and mechanism are shown below in Scheme 1:

Table 1. Results of photocatalytic selective hydrogenation of 3-NS to 3-VA performance for P25-TiO_2 catalysts treated with difference calcination condition under UV light irradiated for 6 h.

Sample	%Conversion of 3-NS	%Selectivity to 3-VA	Rate of 3-VA Formed (μmole/g^{-1}h^{-1})	Rate of Acetone Formed (μmole/g^{-1}h^{-1})
P25	45.4	96.7	74.2	208.3
P25-600-air	43.1	100	71.7	210.5
P25-700-air	70.9	100	120.0	340.0
P25-800-air	57.8	100	99.2	287.4
P25-900-air	51.5	100	87.0	240.6
P25-700-N_2	57.6	100	96.9	288.6
P25-700-H_2	61.4	100	103.3	290.0

$$TiO_2 + h\nu \quad \rightarrow \quad TiO_2\,(e^- + h^+) \tag{1}$$

$$TiO_2\,\{h^+\} + (CH_3)_2CHOH \quad \rightarrow \quad TiO_2\,\{e^-\} + (CH_3)_2CO + 2H^+ \tag{2}$$

$$2TiO_2\,\{e^-\} + (C_8H_7NO_2) + 2H^+ \quad \rightarrow \quad 2TiO_2 + (C_8H_7NO) + H_2O \tag{3}$$

$$2TiO_2\,\{e^-\} + (C_8H_7NO) + 2H^+ \quad \rightarrow \quad 2TiO_2 + (C_8H_9NO) \tag{4}$$

$$2TiO_2\,\{e^-\} + (C_8H_9NO) + 2H^+ \quad \rightarrow \quad 2TiO_2 + (C_8H_7NH_2) + H_2O \tag{5}$$

Scheme 1. Simplified reaction pathways in the hydrogenation of 3-NS.

2.2. Characteristics of the P25-TiO₂ Catalysts

The properties of P25-TiO$_2$ catalysts were modified by heat treatment under various temperatures and gas flows. The XRD patterns of P25-TiO$_2$ after calcination at various conditions are shown in Figure 1. The average crystallite size and rutile content of all the treated TiO$_2$ catalysts were calculated by using Debye-Scherrer's equation and Spurr's method; the results are summarized in Table 2. The P25-TiO$_2$ catalyst presented the characteristic main peaks for anatase (101) phase at 2Θ degrees = 25.3° and rutile (110) phase at 2Θ degrees = 27.4° [19]. P25-TiO$_2$ is a commercial titanium dioxide with 80% anatase and 20% rutile phase components. After calcination at 600 °C, the peaks of the anatase and rutile phases increased correspondingly with slight rise of the rutile phase content from 17% to 27%. However, calcination at higher temperatures caused rapid increase of the rutile phase and crystallite size [20,21]. For example, calcination at 700 °C resulted in rapid phase transformation, and 77% of the rutile phase was formed. The anatase phase was completely transformed when the calcination temperature was further increased to 800 °C. Increase of calcination temperature influenced phase composition and crystallization. The calcination at high temperatures leads to phase transformation of anatase to rutile and crystal growth [20,21]. Changing the calcination atmosphere from air to N$_2$ did not alter the phase transformation and crystal growth; however, calcination in H$_2$ resulted in higher rutile phase content. This was probably due to reduction reaction between H$_2$ gas and TiO$_2$ surface, which created an oxygen vacancy and promoted rutile phase transformation. Formation of point defect under the thermal treatment of TiO$_2$ in a reducing environment accelerated the TiO$_2$ lattice rearrangement process, which promoted the rutile phase transformation [22]. After the heat treatment process, the XRD peak intensity of TiO$_2$ became higher, which indicated that the increase of crystallinity was caused by a re-arrangement of the TiO$_2$ crystal structure.

Table 2. Phase composition, crystallite size, BET surface area, and band gap of P25-TiO₂ calcined difference temperature.

Sample	W_A (%)	W_R (%)	d_A (nm)	d_R (nm)	BET Surface Area (m²/g)	Band Gap (eV)
P25	83	17	23	33	40	3.18
P25-600-air	73	27	29	59	31	3.14
P25-700-air	23	77	43	76	9	3.05
P25-800-air	-	100	-	92	6	3.01
P25-900-air	-	100	-	>100	5	2.98
P25-700-N₂	24	76	40	85	10	3.06
P25-700-H₂	11	89	27	81	9	3.07
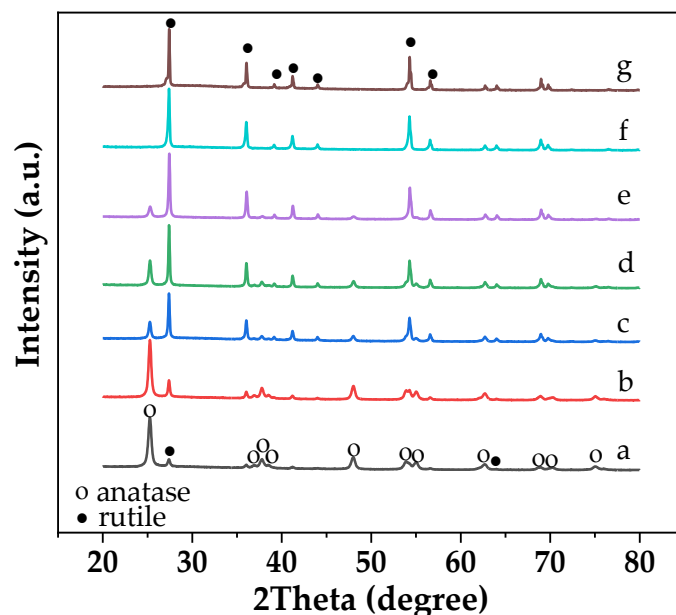
Figure 1. XRD patterns of P25-TiO$_2$ after heat treatment; P25 (**a**), P25-600-air (**b**), P25-700-air (**c**), P25-700-N$_2$ (**d**), P25-700-H$_2$ (**e**), P25-800-air (**f**), P25-900-air (**g**).

The plot between the BET surface area and rutile phase content, which was obtained from the different calcination conditions, is shown in Figure 2. An opposite trend between BET surface area and rutile phase content was clearly observed. P25-TiO$_2$ has surface area of 40 m^2/g. Calcination at a high temperature led to the reduction of surface area and increased rutile component [23]. However, changing calcination atmosphere from air to H$_2$ and N$_2$ did not change the BET surface area.
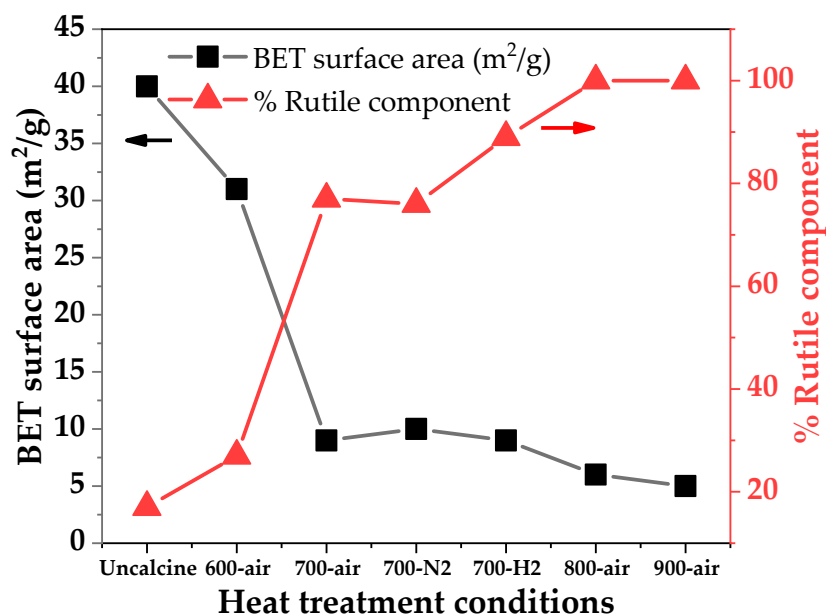
Figure 2. Temperature for heat treatment versus BET surface area and % rutile component.

The UV-Vis absorption and UV-Vis-DR spectra are used to investigate the light adsorption of all treated TiO$_2$ samples at UV and visible light range; the results are shown in Figure 3. The typical band of P25-TiO$_2$ was found at 392 nm, which could be ascribed to the absorption of light caused by the excitation of electron transfer from the valence band to the conduction band [21]. Increasing of calcination temperature resulted in enhancement of visible light adsorption (λ > 400 to 700 nm) and

sharpness of the UV-vis curve (steep slope), which indicated a higher degree of crystalline quality. This was in good agreement with the XRD results. The band gap energy of various treated TiO_2 catalysts can be determined from a plot of $(hv\alpha)^{1/2}$ versus photon energy (hv), which is shown in Figure 4 and Table 2. The redshift in band gap energy of TiO_2 was observed by treatment at a higher temperature due to the increase of rutile phase content in the TiO_2 photocatalysts [21,24,25]. The band gap energy of pure anatase and rutile phase was 3.2 eV and 3.0 eV, respectively [26,27]. Therefore, the increased rutile content after calcination at high temperature narrows the band gap. Moreover, the formation of defects by oxygen loss during the calcination process can lower band gap value of TiO_2, promoting the electron transition from the valence to the conduction band. On the other hand, calcination under different atmospheres did not change main adsorption edge and band gap energy; however, P25-700-H_2 exhibited addition adsorption spectra in the visible light region. Similar results were reported by Naldoni et al. [22,28]. The black TiO_2 obtained from thermal treatment of amorphous commercial TiO_2 in H_2 flow exhibited the adsorption spectra at visible light region. They suggest that the increasing of vacancy site concentration could create a free oxygen vacancy band below the conduction band, which is responsible for visible light absorption.
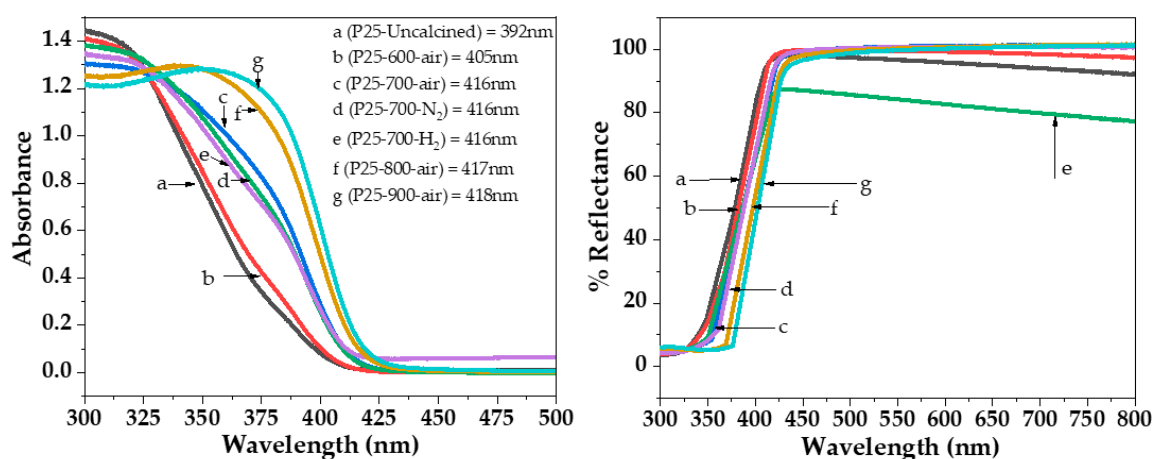
Figure 3. UV-Vis absorption and UV-Vis-DR spectra of P25 (**a**), P25-600-air (**b**), P25-700-air (**c**), P25-700-N_2 (**d**), P25-700-H_2 (**e**), P25-800-air (**f**), P25-900-air (**g**).

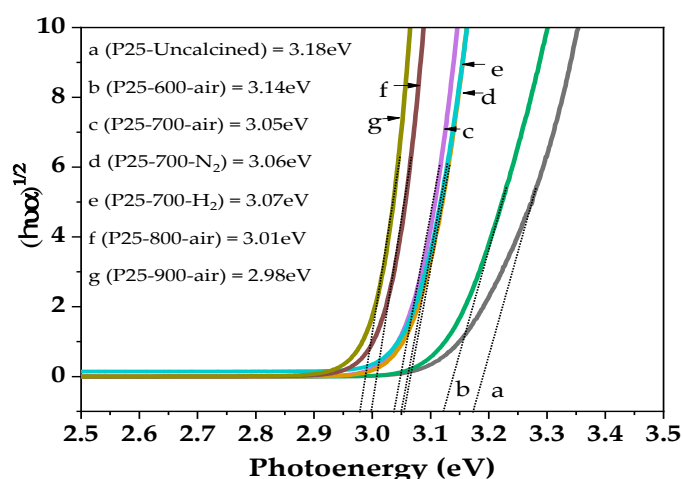**Figure 4.** Band gap plot between $(hv\alpha)^{1/2}$ versus photoenergy of P25 (**a**), P25-600-air (**b**), P25-700-air (**c**), P25-700-N_2 (**d**), P25-700-H_2 (**e**), P25-800-air (**f**), P25-900-air (**g**).

XPS was used to determine the surface properties of treated TiO_2 catalysts. The XPS spectra of Ti 2p of all TiO_2 catalysts are shown in Figure 5. The XPS spectra of TiO_2 exhibited characteristic Ti 2p binding energies, Ti $2p_{3/2}$ and Ti $2p_{1/2}$ doublets, centered at 458.5 eV and 464.5 eV, which were

associated with the Ti^{4+} valence state on lattice oxygen [29–31]. Two shoulder centered at 463 and 457.3 could be assigned to Ti_2O_3, corresponding with the Ti^{3+} valence state and associated with oxygen vacancy (Ov) defect in the system [30–33]. The deconvolution peaks of Ti 2p core levels with Gaussian fitting are also shown in Figure 5. All the treated TiO_2 photocatalysts exhibited four peaks consistent with titanium dioxide (Ti^{4+}) and titanium sub oxide (Ti^{3+}). The surface species' content calculated from the XPS peaks are summarized in Figure 6. The amount of Ti^{3+} did not change after calcination at different temperatures, whereas calcination in reduction atmosphere resulted in an increase of Ti^{3+}. However, the Ti^{3+} contents of all treated TiO_2 catalysts were quite small, which was to attributed the oxidation of Ti^{3+} in air.
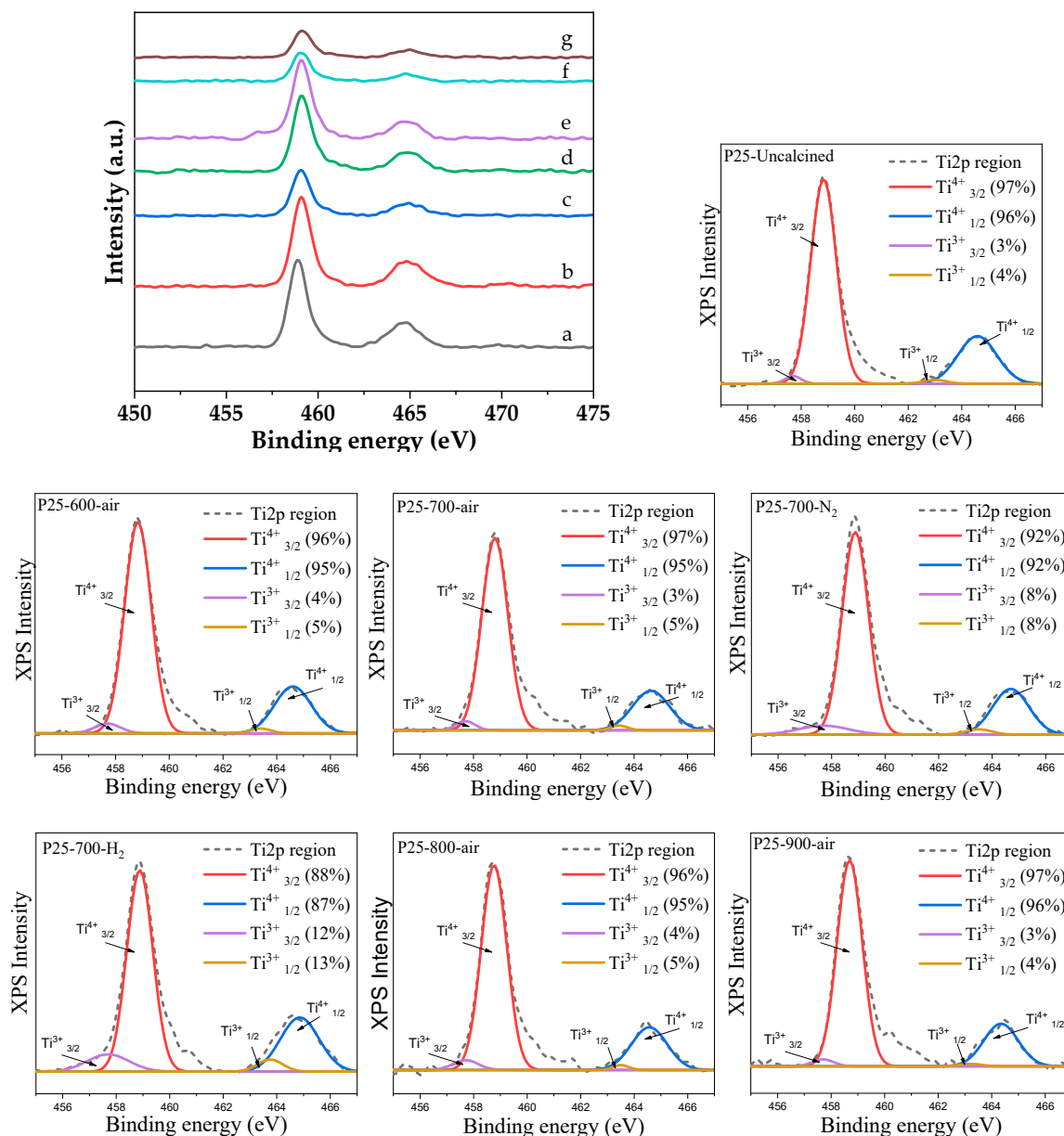

Figure 5. XPS spectra Ti2p of P25-TiO_2 after heat treatment; P25 (**a**), P25-600-air (**b**), P25-700-air (**c**), P25-700-N_2 (**d**), P25-700-H_2 (**e**), P25-800-air (**f**), P25-900-air (**g**).
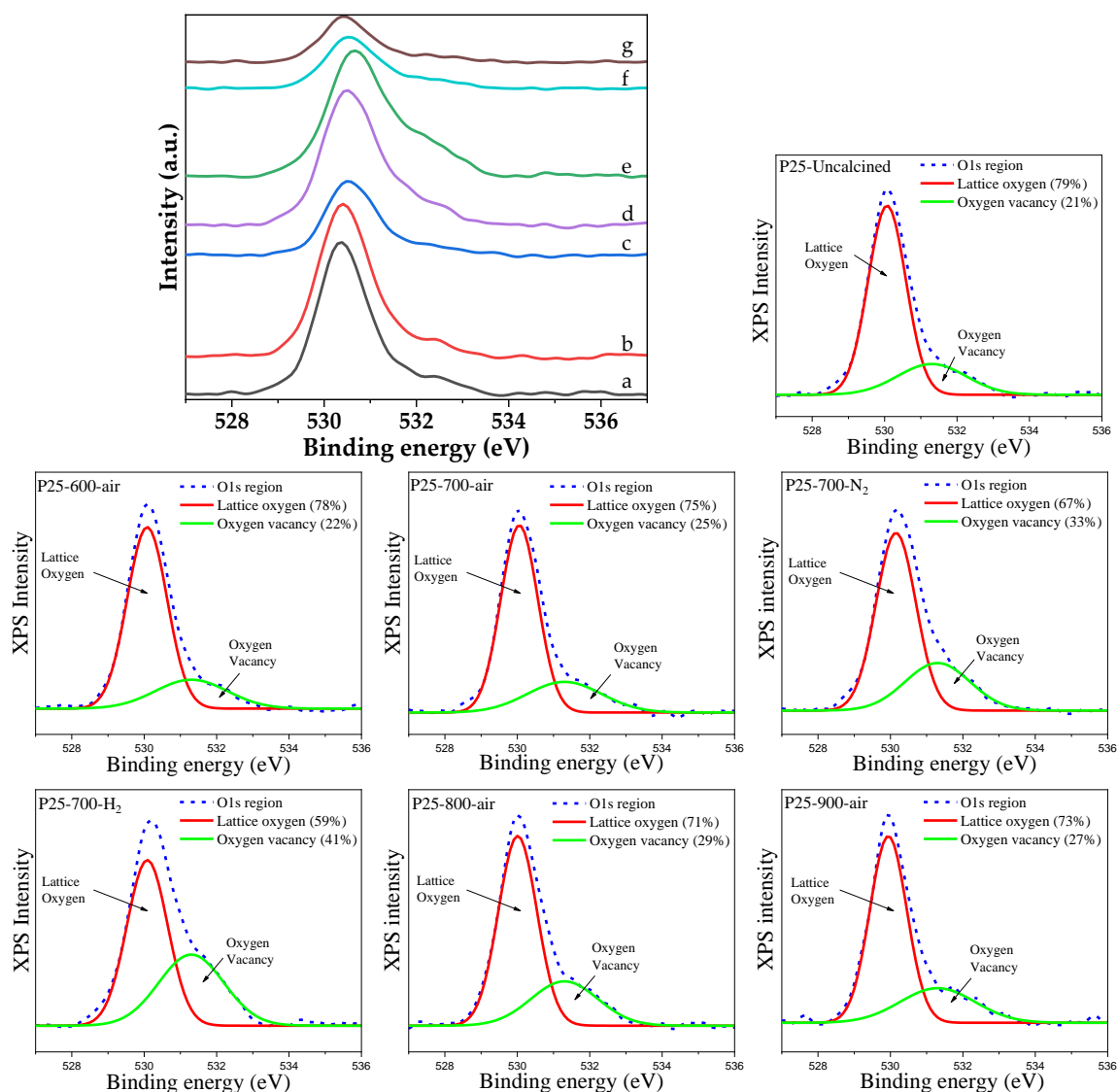
Figure 6. XPS spectra O1s of P25-TiO$_2$ after heat treatment; P25 (**a**), P25-600-air (**b**), P25-700-air (**c**), P25-700-N$_2$ (**d**), P25-700-H$_2$ (**e**), P25-800-air (**f**), P25-900-air (**g**).

The XPS spectra and fitting peaks of O1s core levels of all treated TiO$_2$ catalysts are shown in Figure 6. All the catalysts exhibited two main peaks centered at 529.80 eV and 531.30 eV, which were assigned to the lattice oxygen and Ti$_2$O$_3$-oxygen vacancies sites, respectively [30,31,33,34]. The oxygen surface specie contents, calculated from the deconvolution of XPS spectra, are also summarized in Figure 6. The oxygen vacancy sites slightly increased when the calcination temperature was increased from 600 °C to 800 °C and then remained constant, while, a large increase of oxygen vacancy sites was observed for the ones calcined in N$_2$ and H$_2$. The slight increase of lattice oxygen vacancy sites with calcination in air at high temperature was brought down due to thermal stress caused by rapid change in the calcination process [29]. However, a large increase of oxygen vacancy sites after treatment in a more reduced atmosphere (N$_2$ and H$_2$) was due to the reduction of surface lattice oxygen, which created more oxygen vacancy [32]. A loss of surface lattice oxygen atoms removed from stoichiometric TiO$_2$ affected the Ti^{4+} ions, which received electrons from lattice oxygen, resulting in the increase of the Ti^{3+}/Ti^{4+} ratio.

The efficiency of charge carrier trapping, immigration, and transfer in a semiconductor was investigated by photoluminescence spectroscopy. The PL spectra of all treated TiO$_2$ are shown in Figure 7. Generally, when semiconductor materials receive energy equal or higher to their band

gap, the electrons are excited and then transferred from the valence band to the conduction band, which generates h$^+$ in the valance band. However, electron in the conduction band is easily transferred to the valance band, through a so-called recombination process [35]. The PL signal was energy release photoluminescence during recombination of electron and hole, when electrons transfer from the conduction band bottom to the sub-band; then, the radiative transitions to the valance band, releasing high photoluminescence energy, which results in a high recombination rate [33]. Multiple PL signals can be detected in the visible region. The peak at 436 was attributed to self-trapped electrons localized on TiO$_6$ octahedra [36] and peaks at 451 nm, 469 nm, 484 nm, and 492 nm were attributed to oxygen vacancies with two trapped electrons forming at the TiO$_2$ surface [37–39]. Our results show that the PL spectra decreased drastically as the calcination temperature increased to 700 °C; however, further increasing of calcination temperature resulted in a rise of PL signal. Changes in the calcination atmosphere also affected the PL signal and the signal decreased in order of Air < H$_2$ < N$_2$.
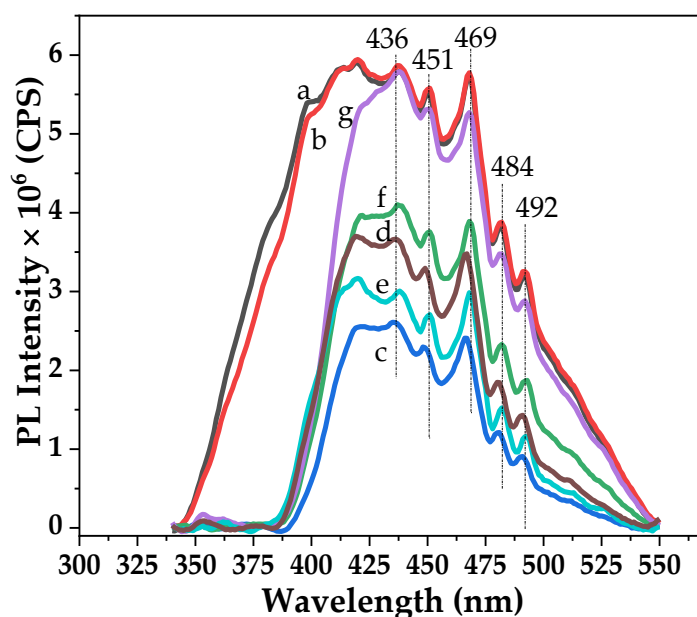

Figure 7. Photoluminescence spectra of P25 (**a**), P25-600-air (**b**), P25-700-air (**c**), P25-700-N$_2$ (**d**), P25-700-H$_2$ (**e**), P25-800-air (**f**), P25-900-air (**g**).

In order to understand the effect of various properties of TiO$_2$ on the catalytic performances in photocatalytic liquid-phase selective hydrogenation of 3-nitrostyrene to 3-vinylaniline, the relationship between the reaction rate of 3-NS and various properties such as crystallite size, %Ti^{3+}, %Oxygen vacancy sites, band gap energy and PL intensity are investigated and shown by different plots in Figure 8. There were no obvious relationships between the reaction rate of 3-NS and those properties, except for the PL intensity. A linear relationship between the reaction rate of 3-NS and PL intensity was clearly observed. This indicates that the electron-hole recombination process was the main factor in this reaction. This is in good agreement with our previous proposed reaction mechanism. The photocatalytic selective hydrogenation of 3-NS did not require the metal sites to hydrogenate substrates like conventional liquid phase selective hydrogenation; however, the H$^+$, generated by a reaction between isopropanol and hole (h$^+$) and electron, were necessary for the 3-VA formation. The electron and hole (h$^+$) required in this process were generated from the photoreaction. Therefore, the electron and hole separation process directly affects the photocatalytic activity in selective hydrogenation of 3-NS.
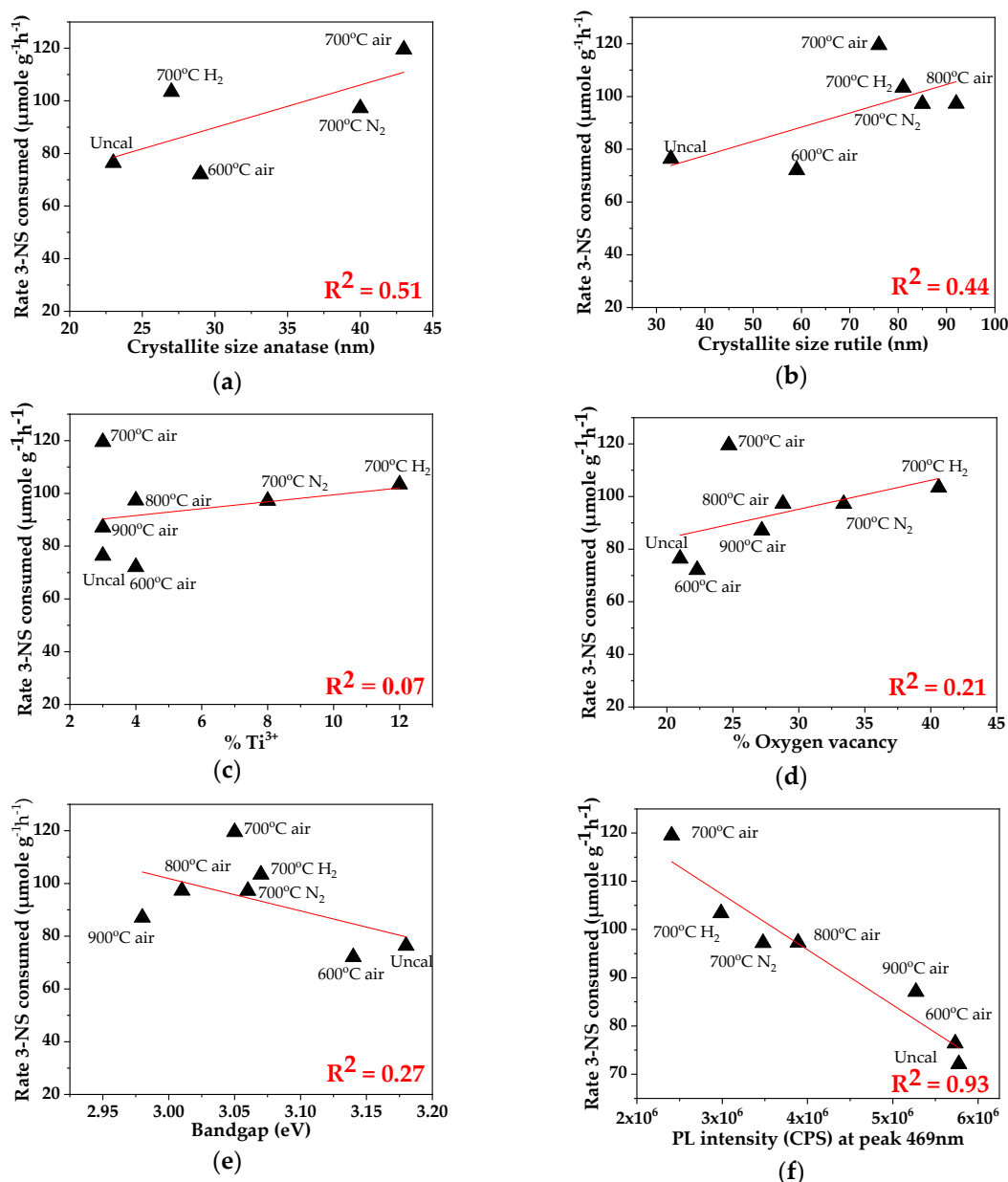
Figure 8. Rate of 3-NS formed versus properties after heat treatment of P25-TiO$_2$; crystallite size anatase (**a**), crystallite size rutile (**b**), %Ti^{3+} (**c**), %Oxygen vacancy (**d**), bandgap (**e**), PL intensity at peak 469 nm (**f**).

The obtained results show that the %3-NS conversion increased from 45.4 to 70.9 after calcination at 700 °C; however, further increasing of calcination temperature to 800 °C and 900 °C resulted in a decrease of %3-NS conversion to 57.8 and 51.5, respectively. The characterization results show that increasing of calcination temperature resulted in increase of crystallite size, rutile content, crystallinity, oxygen vacancy content, and narrow band gap. Improvement of TiO$_2$ crystallinity after calcination reduces the electron–hole pair loss, owing to the trapping of either charge carriers at defect states [11]. The presence of mix phases of anatase and rutile in the TiO$_2$ catalysts also promoted photocatalytic activity by a synergistic effect between the antenna effect of rutile phase, which had a stronger photoabsorption and provided more electron-hole pairs; and the activation effect by anatase phase, which reduces the recombination of photogenerated charges [40–46]. However, increasing of crystallite size after calcination resulted in a decrease of the surface area of TiO$_2$, which reduced the density of active sites for substrate adsorption [21]. In our case, calcination at 700 °C cured the TiO$_2$ crystal

defect and provided rutile phase contents, which reduced the electron-hole recombination process by a synergistic effect. However, calcination at a higher temperature resulted in the complete transformation of anatase to rutile phase and large increase of the TiO_2 crystallite size, leading to the loss of synergistic effect of the mix phases and the loss of active surface area of the photocatalysts.

Calcination under various atmospheres at the same temperature did not have much effect on physical and optical properties, such as BET surface area, crystallite size, rutile content, and band gap energy, except higher rutile content and broad band absorption for $\lambda > 400$ nm after calcination in H_2 flows; however, it could alter the surface Ti^{3+} and oxygen vacancy sites. The Ti^{3+} and oxygen vacancy site on the TiO_2 surface are known as an active site to trapp nitroaromatic at the conduction band [2,16] and increase the separation of the charge carriers. However, the PL results showed that the recombination process were in order of Air $< H_2 < N_2$, which was similar in trend to the photocatalytic activity. This suggests that the excess of Ti^{3+} and oxygen vacancy site led to the formation of the un-localize band at the conduction band, leading to faster recombination [47–52].

2.3. Recyclability and Properties of Spent Catalysts

In order to determine the stability and recyclability of the catalysts, the photocatalytic selective hydrogenation performance of the P25-700-air catalyst was repeatedly determined for five consecutive batches. The catalysts were recovered by using centrifugation and filtration from the obtained reaction mixture and then re-used. As shown in Figure 9, it is clear that only negligible loss (less than 13%) in %3-NS conversion was observed. This suggests that the prepared photocatalyst is active and can be used for long-term applications.
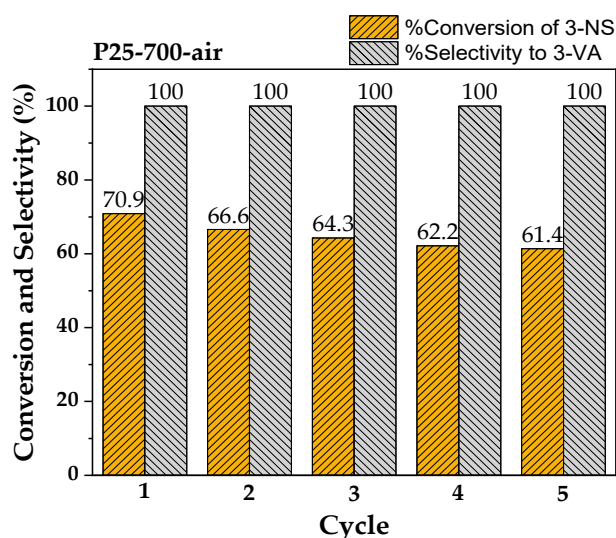

Figure 9. The catalytic performance of P25-700-air under UV light irradiated for 6 h at different cycles.

The physiochemical properties of spent catalysts were evaluated using TGA analysis; the results are presented in Figure 10. All the spent catalysts exhibited %weight loss in the range of 0.8% to 5%, and a temperature range of 100 °C to 500 °C. This weight loss could probably be due to the thermal decomposition or volatilization of chemical substance presented in the TiO_2 catalysts [53,54]. However, the weight loss that occurred at a higher temperature can be attributed the condensation reaction between two adjacent Ti–OH groups, which resulted in the formation of Ti–O–Ti bonds and loss of water molecules [55]. These processes were associated with crystal growth and the rutile phase transformation process. The amount of %weight loss decreased as the calcination temperature increased, due to fact that the chemical substance and loss of water had already occurred after thermal treatment.
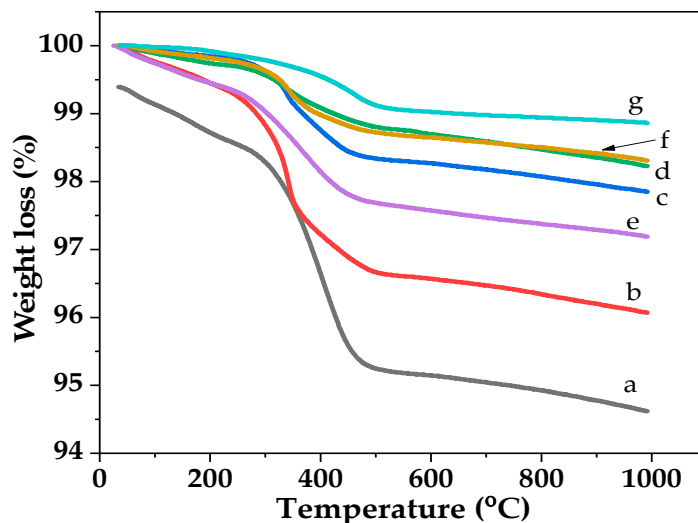
Figure 10. TGA analysis of all spent catalysts; P25 (**a**), P25-600-air (**b**), P25-700-air (**c**), P25-700-N$_2$ (**d**), P25-700-H$_2$ (**e**), P25-800-air (**f**), P25-900-air (**g**).

3. Materials and Methods

3.1. Synthesis of Treated P25-TiO$_2$

Degussa P25-TiO$_2$ (Commercial TiO$_2$) was used as the reference catalyst. Two gram of P25-TiO$_2$ was transferred into the crucible and calcinated at various temperatures in a muffle furnace for 5 h, resulting in P25-xxx-air (xxx = 600, 700, 800, 900 °C). P25-xxx-H$_2$, P25-xxx-N$_2$ were calcinated in H$_2$ and N$_2$ gas flow, respectively, for 5 h.

3.2. Photocatalytic Test

200 μmol of 3-nitrostyrene (96%, Aldrich Chem. CO. Ltd, Darmstadt, HE, Germany), 20 mL of isopropanol (99.95%, Fisher Chem. CO. Ltd, Pittsburgh, PA, USA) and 0.2 g of catalyst were transferred into a pyrex glass tube reactor and sealed by septum. The mixture was sonicated for 5 min to disperse catalysts in the solution. The solution was purged by introducing N$_2$ bubble gas for 5 min, which eliminated air from the reactor. The pyrex glass tube containing the substrate, solvent and catalyst were photo-irradiated under mercury mixed lamp Philips 500 W E40) for 6 h, which was located 10 cm above the suspension surface, with a magnetic stirrer. The substrate and products were analyzed by GC-FID, which was calibrated with authentic concentrations of both samples. After the reaction, the catalyst was removed by filtration and the resulting products analyzed by GC-FID Shimadzu (with Rtx®5 Restek columns, Bellefonte, PA, USA and DB-1wax Agilent columns, Santa Clara, CA, USA).

3.3. Analytical Method

All powder characterizations were investigated at room temperature. The X-ray diffraction (XRD) was estimated by a SIEMENS D5000 X-ray diffractometer (Berlin, Germany) with Cu Kα radiation using an Ni filter. The BET surface area was measured through single-point nitrogen gas physical adsorption using the Micromeritics Chemisorb 2750 Pulse Chemisorption System (Norcross, GA, USA). X-ray photoelectron spectroscopy (XPS) was performed by an AMICUS photoelectron spectrometer (Manchester, UK) equipped with a Mg Kα that had X-ray as a primary excitation and a KRATOS VISION2 software. UV-Vis spectroscopy was performed by using the Perkin Elmer Lambda 650 spectrophotometer (Waltham, MA, USA). The photoluminescence spectroscopy (PL) was achieved using Fluromax® by Horiba and Xenon lamp source excitation at 320 nm (Minami-ku Kyoto, Japan).

Thermogravimetric analysis was done with air by using SDT Q600 V8.3 Build 101 (New Castle, DE, USA).

4. Conclusions

Photocatalytic selective hydrogenation of 3-NS to 3-VA was carried out in a suspension of TiO_2 photocatalysts in isopropanol under UV-light irradiation. The effect of TiO_2 properties on photocatalytic performances were investigated by treating the P25-TiO_2 at different calcination temperatures under different gases flows (H_2, N_2, and Air). A linear correlation between the reaction rate of 3-NS and PL intensity was clearly observed. This suggests that the electron-hole recombination process was the main factor in this reaction. Among all the catalysts studied, the P25-700-air exhibited the highest photocatalytic activity due to its high crystallinity and optimum amount of mixed phase content, leading to the reduction of the electron-hole recombination process by a synergistic effect.

Author Contributions: Conceptualization, O.M. and P.P.; Methodology, O.M. and P.P.; Investigation, S.C.; Data Collection, S.C.; Writing-Original Draft Preparation, S.C. and O.M.; Writing-Review & Editing, O.M. and J.P.; Supervision, P.P.; Project Administration, P.P.; Funding Acquisition, P.P.

Conflicts of Interest: The authors declare no conflict of interest.

References

1. Berguerand, C. Chemoselective Liquid Phase Hydrogenation of 3-Nitrostyrene over Pt Nanoparticles: Synergy with ZnO Support. *Ind. Eng. Chem. Res.* **2015**, *54*, 8659–8669. [CrossRef]

2. Shiraishi, Y.; Togawa, Y.; Tsukamoto, D.; Tanaka, S.; Hirai, T. Highly Efficient and Selective Hydrogenation of Nitroaromatics on Photoactivated Rutile Titanium Dioxide. *ACS Catal.* **2012**, *2*, 2475–2481. [CrossRef]

3. Pisduangdaw, S.; Mekasuwandumrong, O.; Yoshida, H.; Fujita, S.-I.; Arai, M.; Panpranot, J. Flame-made Pt/TiO_2 catalysts for the liquid-phase selective hydrogenation of 3-nitrostyrene. *Appl. Catal. A* **2015**, *490*, 193–200. [CrossRef]

4. Pisduangdaw, S.; Mekasuwandumrong, O.; Fujita, S.-I.; Arai, M.; Yoshida, H.; Panpranot, J. One step synthesis of Pt–Co/TiO_2 catalysts by flame spray pyrolysis for the hydrogenation of 3-nitrostyrene. *Catal. Commun.* **2015**, *61*, 11–15. [CrossRef]

5. Nuzhdin, A.L.; Reshetnikov, S.I.; Bukhtiyarova, G.A.; Moroz, B.L.; Gerasimov, E.Y.; Pyrjaev, P.A.; Bukhtiyarov, V.I. Study of Catalyst deactivation in liquid-phase hydrogenation of 3-nitrostyrene over Au/Al_2O_3 catalyst in flow reactor. *Catal. Lett.* **2017**, *147*, 572–580. [CrossRef]

6. Fujita, S.-I.; Yoshida, H.; Asai, K.; Meng, X.; Arai, M. Selective hydrogenation of nitrostyrene to aminostyrene over Pt/TiO_2 catalysts: Effects of pressurized carbon dioxide and catalyst preparation conditions. *J. Supercrit. Fluids* **2011**, *60*, 106–112. [CrossRef]

7. Corma, A.; Serna, P.; Concepcion, P.; Calvino, J.J. Transforming nonselective into chemoselective metal catalysts for the hydrogenation of substituted nitroaromatics. *J. Am. Chem. Soc.* **2008**, *130*, 8748–8753. [CrossRef] [PubMed]

8. Beier, M.J.; Andanson, J.-M.; Baiker, A. Tuning the chemoselective hydrogenation of nitrostyrenes catalyzed by ionic liquid-supported platinum nanoparticles. *ACS Catal.* **2012**, *2*, 2587–2595. [CrossRef]

9. Yoshida, H.; Igarashi, N.; Fujita, S.-I.; Panpranot, J.; Arai, M. Influence of crystallite size of TiO_2 supports on the activity of dispersed Pt catalysts in liquid-phase selective hydrogenation of 3-nitrostyrene, nitrobenzene, and styrene. *Catal. Lett.* **2015**, *145*, 606–611. [CrossRef]

10. Makosch, M.; Lin, W.-I.; Bumbálek, V.; Sá, J.; Medlin, J.W.; Hungerbühler, K.; van Bokhoven, J.A. Organic thiol modified Pt/TiO_2 catalysts to control chemoselective hydrogenation of substituted nitroarenes. *ACS Catal.* **2012**, *2*, 2079–2081. [CrossRef]

11. Paz, Y. Application of TiO_2 photocatalysis for air treatment: Patents' overview. *Appl. Catal. B* **2010**, *99*, 448–460. [CrossRef]

12. Fukahori, S.; Ichiura, H.; Kitaoka, T.; Tanaka, H. Capturing of bisphenol A photodecomposition intermediates by composite TiO_2–zeolite sheets. *Appl. Catal. B* **2003**, *46*, 453–462. [CrossRef]

13. Maness, P.C.; Smolinski, S.; Blake, D.M.; Huang, Z.; Wolfrum, E.J.; Jacoby, W.A. Bactericidal Activity of Photocatalytic TiO_2 Reaction: Toward an Understanding of Its Killing Mechanism. *Appl. Environ. Microbiol.* **1999**, *65*, 4094–4098.

14. Liou, J.W.; Chang, H.H. Bactericidal effects and mechanisms of visible light-responsive titanium dioxide photocatalysts on pathogenic bacteria. *Arch. Immunol. Ther. Exp.* **2012**, *60*, 267–275. [CrossRef] [PubMed]

15. Sano, T.; Negishi, N.; Koike, K.; Takeuchi, K.; Matsuzawa, S. Preparation of a visible light-responsive photocatalyst from a complex of Ti49+ with a nitrogen-containing ligand. *J. Mater. Chem.* **2004**, *14*, 380–384. [CrossRef]

16. Imamura, K.; Yoshikawa, T.; Hashimoto, K.; Kominami, H. Stoichiometric production of aminobenzenes and ketones by photocatalytic reduction of nitrobenzenes in secondary alcoholic suspension of titanium(IV) oxide under metal-free conditions. *Appl. Catal. B* **2013**, *134–135*, 193–197. [CrossRef]

17. Imamura, K.; Iwasaki, S.; Maeda, T.; Hashimoto, K.; Ohtani, B.; Kominami, H. Photocatalytic reduction of nitrobenzenes to aminobenzenes in aqueous suspensions of titanium(IV) oxide in the presence of hole scavengers under deaerated and aerated conditions. *Phys. Chem. Chem. Phys.* **2011**, *13*, 5114–5119. [CrossRef] [PubMed]

18. Imamura, K.; Hashimoto, K.; Kominami, H. Chemoselective reduction of nitrobenzenes to aminobenzenes having reducible groups by a titanium(IV) oxide photocatalyst under gas- and metal-free conditions. *Chem. Commun.* **2012**, *48*, 4356–4358. [CrossRef]

19. Bhosale, R.; Hyam, R.; Dhanya, P.; Ogale, S. Chlorate ion mediated rutile to anatase reverse phase transformation in the TiO_2 nanosystem. *Dalton Trans.* **2011**, *40*, 11374–11377. [CrossRef]

20. Fernandes Machado, N.R.C.; Santana, V.S. Influence of thermal treatment on the structure and photocatalytic activity of TiO_2 P25. *Catal. Today* **2005**, *107–108*, 595–601. [CrossRef]

21. Wang, G.; Xu, L.; Zhang, J.; Yin, T.; Han, D. Enhanced Photocatalytic Activity of Powders (P25) via Calcination Treatment. *Int. J. Photoenergy* **2012**, *2012*, 1–9. [CrossRef]

22. Naldoni, N.; Allieta, M.; Santangelo, S.; Marelli, M.; Fabbri, F.; Cappelli, S.; Bianchi, C.L.; Psaro, R.; Dal Santo, V. The effect of nature and location of defects on bandgap narrowing in black TiO_2 nanoparticles. *J. Am. Chem. Soc.* **2012**, *134*, 7600–7603. [CrossRef]

23. Park, G.C.; Seo, T.Y.; Park, C.H.; Lim, J.H.; Joo, J. Effects of Calcination Temperature on Morphology, Microstructure, and Photocatalytic Performance of TiO_2 Mesocrystals. *Ind. Eng. Chem. Res.* **2017**, *56*, 8235–8240. [CrossRef]

24. Saputera, W.H.; Mul, G.; Hamdy, M.S. Ti3+-containing titania: Synthesis tactics and photocatalytic performance. *Catal. Today* **2015**, *246*, 60–66. [CrossRef]

25. Yuangpho, N.; Le, S.T.T.; Treerujiraphapong, T.; Khanitchaidecha, W.; Nakaruk, A. Enhanced photocatalytic performance of TiO_2 particles via effect of anatase–rutile ratio. *Phys. E* **2015**, *67*, 18–22. [CrossRef]

26. Reyes-Coronado, D.; Rodriguez-Gattorno, G.; Espinosa-Pesqueira, M.E.; Cab, C.; de Coss, R.; Oskam, G. Phase-pure TiO(2) nanoparticles: Anatase, brookite and rutile. *Nanotechnology* **2008**, *19*, 145605. [CrossRef] [PubMed]

27. Leal, J.H.; Cantu, Y.; Gonzalez, D.F.; Parsons, J.G. Brookite and anatase nanomaterial polymorphs of TiO_2 synthesized from $TiCl_3$. *Inor. Chem. Commun.* **2017**, *84*, 28–32. [CrossRef]

28. Naldoni, A.; Riboni, F.; Marelli, M.; Bossola, F.; Ulisse, G.; Carlo, A.D.; Píš, I.; Nappini, S.; Malvestuto, M.; Dozzi, M.V.; Psaro, R.; et al. Influence of TiO_2 electronic structure and strong metal–support interaction on plasmonic Au photocatalytic oxidations. *Catal. Sci. Technol.* **2016**, *6*, 3220–3229. [CrossRef]

29. Bharti, B.; Kumar, S.; Lee, H.N.; Kumar, R. Formation of oxygen vacancies and Ti(3+) state in TiO_2 thin film and enhanced optical properties by air plasma treatment. *Sci. Rep.* **2016**, *6*, 32355. [CrossRef]

30. Tshabalala, Z.P.; Motaung, D.E.; Mhlongo, G.H.; Ntwaeaborwa, O.M. Facile synthesis of improved room temperature gas sensing properties of TiO_2 nanostructures: Effect of acid treatment. *Sens. Actuators B Chem.* **2016**, *224*, 841–856. [CrossRef]

31. Paul, K.K.; Jana, S.; Giri, P.K. Tunable and High Photoluminescence Quantum Yield from Self-Decorated TiO_2 Quantum Dots on Fluorine Doped Mesoporous TiO_2 Flowers by Rapid Thermal Annealing. *Part. Part. Syst. Charact.* **2018**, *35*, 1800198. [CrossRef]

32. Xiong, L.-B.; Li, J.-L.; Yang, B.; Yu, Y. Ti3+ in the Surface of Titanium Dioxide: Generation, Properties and Photocatalytic Application. *J. Nanomater.* **2012**, *2012*, 1–13. [CrossRef]

33. Wang, X.; Li, Y.; Liu, X.; Gao, S.; Huang, B.; Dai, Y. Preparation of Ti3+ self-doped TiO$_2$ nanoparticles and their visible light photocatalytic activity. *Chin. J. Catal.* **2015**, *36*, 389–399. [CrossRef]

34. Wang, X.; Wang, X.; Di, Q.; Zhao, H.; Liang, B.; Yang, J. Mutual Effects of Fluorine Dopant and Oxygen Vacancies on Structural and Luminescence Characteristics of F Doped SnO(2) Nanoparticles. *Materials* **2017**, *10*, 1398. [CrossRef] [PubMed]

35. Jing, L. Review of photoluminescence performance of nano-sized semiconductor materials and its relationships with photocatalytic activity. *Sol. Energy Mater. Sol. Cells* **2006**, *90*, 1773–1787.

36. Khan, H.; Berk, D. Effect of a Chelating Agent on the Physicochemical Properties of TiO$_2$: Characterization and Photocatalytic Activity. *Catal. Lett.* **2014**, *144*, 890–904. [CrossRef]

37. Hou, C.; Liu, W. One-step synthesis of OH-TiO$_2$/TiOF$_2$ nanohybrids and their enhanced solar light photocatalytic performance. *R. Soc. Open Sci.* **2018**, *5*, 172005. [CrossRef] [PubMed]

38. Jiang, Y.; Yang, Z.; Zhang, P.; Jin, H.; Ding, Y. Natural assembly of a ternary Ag–SnS–TiO$_2$ photocatalyst and its photocatalytic performance under simulated sunlight. *RSC Adv.* **2018**, *8*, 13408–13416. [CrossRef]

39. Verma, V.; Samanta, S.K. Degradation kinetics of pollutants present in a simulated wastewater matrix using UV/TiO$_2$ photocatalysis and its microbiological toxicity assessment. *Res. Chem. Intermediat.* **2017**, *43*, 6317–6341. [CrossRef]

40. Su, R.; Bechstein, R.; Lasse, S.; Vang, R.T.; Sillassen, M.; Esbjörnsson, B.; Palmqvist, A.; Besenbacher, F. How the Anatase-to-Rutile Ratio Influences the Photoreactivity of TiO$_2$. *J. Phys. Chem. C* **2011**, *115*, 24287–24292. [CrossRef]

41. Bakardjieva, S.; Šubrt, J.; Štengl, V.; Dianez, M.J.; Sayagues, M.J. Photoactivity of anatase–rutile TiO$_2$ nanocrystalline mixtures obtained by heat treatment of homogeneously precipitated anatase. *Appl. Catal. B* **2005**, *58*, 193–202. [CrossRef]

42. Fu, W. Facile formation of mesoporous structured mixed-phase (anatase/rutile) TiO$_2$ with enhanced visible light photocatalytic activity. *Chem. Commun.* **2017**, *54*, 58–61. [CrossRef] [PubMed]

43. Choudhury, B.; Choudhury, A. Oxygen defect dependent variation of band gap, Urbach energy and luminescence property of anatase, anatase–rutile mixed phase and of rutile phases of TiO$_2$ nanoparticles. *Phys. E* **2014**, *56*, 364–371. [CrossRef]

44. Wang, W.K.; Chen, J.J.; Zhang, X.; Huang, Y.X.; Li, W.W.; Yu, H.Q. Self-induced synthesis of phase-junction TiO$_2$ with a tailored rutile to anatase ratio below phase transition temperature. *Sci. Rep.* **2016**, *6*, 20491. [CrossRef] [PubMed]

45. Komaguchi, K.; Nakano, H.; Araki, A.; Harima, Y. Photoinduced electron transfer from anatase to rutile in partially reduced TiO$_2$ (P-25) nanoparticles: An ESR study. *Chem. Phys. Lett.* **2006**, *428*, 338–342. [CrossRef]

46. Mi, Y.; Weng, Y. Band Alignment and Controllable Electron Migration between Rutile and Anatase TiO$_2$. *Sci. Rep.* **2015**, *5*, 11482. [CrossRef] [PubMed]

47. Wang, K.; Kampwerth, H. A Method to Separate Bulk Lifetime and Surface Recombination Velocity of Silicon Bricks based on Transient Photoluminescence. *Energy Procedia* **2014**, *55*, 161–168. [CrossRef]

48. Cong, Y.; Li, B.; Yue, S.; Fan, D.; Wang, X.-J. Effect of Oxygen Vacancy on Phase Transition and Photoluminescence Properties of Nanocrystalline Zirconia Synthesized by the One-Pot Reaction. *J. Phys. Chem. C* **2009**, *113*, 13974–13978. [CrossRef]

49. Gan, J.; Lu, X.; Wu, J.; Xie, S.; Zhai, T.; Yu, M.; Zhang, Z.; Mao, Y.; Wang, S.C.; Shen, Y.; et al. Oxygen vacancies promoting photoelectrochemical performance of In(2)O(3) nanocubes. *Sci. Rep.* **2013**, *3*, 1021. [CrossRef]

50. Kang, Q.; Cao, J.; Zhang, Y.; Liu, L.; Xu, H.; Ye, J. Reduced TiO$_2$ nanotube arrays for photoelectrochemical water splitting. *J. Mater. Chem. A* **2013**, *1*, 5766–5774. [CrossRef]

51. Zhang, F.; Ma, W.; Guo, H.; Zhao, Y.; Shan, X.; Jin, K.; Tian, H.; Zhao, Q.; Yu, D.; Lu, X.; et al. Interfacial Oxygen Vacancies as a Potential Cause of Hysteresis in Perovskite Solar Cells. *Chem. Mater.* **2016**, *28*, 802–812. [CrossRef]

52. Pan, X.; Yang, M.Q.; Fu, X.; Zhang, N.; Xu, Y.J. Defective TiO$_2$ with oxygen vacancies: Synthesis, properties and photocatalytic applications. *Nanoscale* **2013**, *5*, 3601–3614. [CrossRef]

53. Li, D.; Chen, S.; Wang, D.; Li, Y.; Shao, W.; Long, Y.; Liu, Z.; Ringer, S.P. Thermo-analysis of nanocrystalline TiO$_2$ ceramics during the whole sintering process using differential scanning calorimetry. *Ceram. Int.* **2010**, *36*, 827–829. [CrossRef]

54. Souza, I.P.A.F.; Pezoti, O.; Bedin, K.C.; Cazetta, A.L.; Melo, S.A.R.; Souza, L.S.; Silva, M.C.; Almeida, V.C. Chemometric study of thermal treatment effect on the P25 photoactivity for degradation of tartrazine yellow dye. *Ceram. Int.* **2018**, *44*, 12292–12300. [CrossRef]

55. Marinescu, C.; Sofronia, A.; Rusti, C.; Piticescu, R.; Badilita, V.; Vasile, E.; Baies, R.; Tanasescu, S. DSC investigation of nanocrystalline TiO_2 powder. *J. Therm. Anal. Calorim.* **2011**, *103*, 49–57. [CrossRef]